

Cortical Maps and White Matter Tracts following Long Period of Visual Deprivation and Retinal Image Restoration

Netta Levin,^{1,3,*} Serge O. Dumoulin,² Jonathan Winawer,¹ Robert F. Dougherty,¹ and Brian A. Wandell¹

¹Department of Psychology, Stanford University, Stanford, CA 94305-2130, USA

²Helmholtz Institute, Experimental Psychology Division, Utrecht University, Utrecht, Netherlands

³Present address: Department of Neurology, Hadassah Hebrew University Hospital, Jerusalem 91120, Israel

*Correspondence: netta@hadassah.org.il

DOI 10.1016/j.neuron.2009.12.006

SUMMARY

Abnormal visual input during development has dramatic effects on the visual system. How does the adult visual system respond when input is corrected? MM lost his left eye and became blind in the right due to corneal damage at the age of 3. At age 46, MM regained his retinal image, but his visual abilities, even seven years following the surgery, remain severely limited, and he does not rely on vision for daily life. Neuroimaging measurements reveal several differences among MM, sighted controls, sighted monocular, and early blind subjects. We speculate that these differences stem from damage during the critical period in development of retinal neurons with small, foveal receptive fields. In this case, restoration of functional vision requires more than improving retinal image contrast. In general, visual restoration will require accounting for the developmental trajectory of the individual and the consequences of the early deprivation on cortical circuitry.

INTRODUCTION

The possibility of restoring sight to the blind has been of great interest to the scientific community. Retinal prosthetic devices, stem cell transplantation as well as genetic therapies offer the hope of restoring sight, but there remain many unsolved technical problems (Aguirre et al., 2007; Bi et al., 2006; Jacobson et al., 2005; Lagali et al., 2008; Merabet et al., 2005). Beyond the technical limitations, there is also the question of whether long-deprived visual cortex will be able to extract and interpret the relevant visual signals. Can a person re-acquire visual function after being deprived of a retinal image during development?

The manuscript describes a series of anatomical and functional measurements in subject MM, who lost vision in both eyes at age 3. At age 46, the optics was restored in one eye but now, seven years later, MM still has limited visual ability.

The visual pathways are not fully developed in human at 3 years of age. Spatial resolution, as measured behaviorally by grating acuity, is poor at birth (0.5–1 cpd). At 3 years, grating

acuity measured psychophysically and using visual evoked potentials is typically near 25 cpd and reaches adult levels (30–40 cpd) about 3 years later (Mayer and Dobson, 1982; Skoczenski and Norcia, 2002). Positional discrimination, as measured by vernier acuity, reaches adult performance levels much later (10–14 years of age) (Skoczenski and Norcia, 2002). A similar sequence of grating acuity followed by vernier acuity occurs in monkey development, but at an accelerated pace (Kiorpes and Movshon, 1989).

Three groups of studies suggest that visual recovery after a long period of deprivation will be problematic. First, there is a group of behavioral studies in subjects who recovered after long-lasting visual deprivation, but the literature on this issue is rather sparse (Ackroyd et al., 1974; Carlson et al., 1986; Gregory, 1963; Ostrovsky et al., 2006; Valvo, 1971). The main point rising from those reports is that humans who have been blind beyond childhood face great visual difficulties after regaining their visual capabilities. Previously reported psychophysical measurements highlighted that MM's performance on simple color and motion processing was essentially normal while his spatial resolution and judgments of complex forms were severely impaired (Fine et al., 2003). For example, his upper spatial frequency limit is on the order of three cycles per degree (cpd), which is an order of magnitude lower than normal controls.

Second, there is a group of studies showing significant anatomical and functional connectivity changes in deafferented visual cortex. Several groups have shown reduced white matter volumes in the optic tract and optic radiation and sometimes conflicting differences in gray matter in the visual cortex of early blind patients compared to controls (Jiang et al., 2009; Pan et al., 2007; Park et al., 2009; Ptito et al., 2008). Three recent diffusion tensor imaging (DTI)-based studies in the early blind population provide further evidence of abnormalities in the optic radiations; showing an increased diffusivity and decreased anisotropy (Shimony et al., 2006; Shu et al., 2009) and suggesting a compensatory increase in the anisotropy of the corticospinal tracts (in the early blind men but not in women [Yu et al., 2007]). Resting state studies demonstrated decreased functional connectivity within the visual cortex as well as between the occipital lobe and other lobes (Liu et al., 2007).

A third group of studies suggests that recovery from blindness will be problematic because visual cortex in early blind subjects is taken over by other functions. There are reports that visual cortex becomes sensitive to auditory and tactile stimuli (Sadato

et al., 1996; Saenz et al., 2008; Weeks et al., 2000); there are also reports of responses to cognitive processes (Amedi et al., 2003) and a superior performance of the blind in their remaining senses (Pascual-Leone et al., 2005). To the extent that this superior function is explained by reorganization or colonization of the input-deprived visual cortex, attempts to restore sight by retinal stimulation or retinal stem cell implants may be frustrated.

After seven years of restored optics, adult cortical plasticity has not compensated for the loss of these visual signals. To understand the deficit, we made functional (fMRI) and anatomical (DTI and fiber tracking) neuroimaging measurements in MM and several types of controls: normal sighted adults, two sighted monocular subjects, and an early blind subject. We describe several differences between MM and these controls, and we speculate that these differences arise because of a failure of specific parts of the visual system to develop following his injury.

RESULTS

Behaviorally, we confirmed that MM continues to have poor spatial resolution and limited visual abilities, even seven years following his operation (Figure 1). We assess MM's brain by a series of neuroimaging measurements that evaluate cortical maps (fMRI) and white matter structural integrity (diffusion weighted). We speculate that most of the differences between MM and the controls arise from a failure of subpopulations of retinal neurons with small receptive fields to develop during the critical period following the injury.

Cortical Mapping

MM's V1 Eccentricity Map Is Abnormal

MM has an organized eccentricity map in calcarine cortex that differs from controls in several ways (Figure 2; see also Fine et al., 2003). In MM, the most effective visual stimuli are at eccentricities beyond 3 deg, while in visually normal subjects a large portion of cortex around the occipital pole that usually includes posterior calcarine sulcus represents the central few degrees (Figure 2A, right panel). In MM, we were not able to measure an organized eccentricity map in the most posterior portion of the occipital pole or lateral to it (for a lateral view, see Figure 5). This region typically contains a large representation of the central three degrees.

To quantify the function relating position along the calcarine sulcus with visual field eccentricity, we traced the visual field eccentricity map along two V1 paths that represent a constant angle, near the horizontal meridian. In control subjects, eccentricity increases as a function of distance along the cortical surface according to an exponential function (Engel et al., 1997; we arbitrarily assign the representation at 10 deg to a position of 0 mm). There is considerable variance in the size of V1 in human (Dougherty et al., 2003). A large range of functions from controls is shown in Figure 2B (thin gray curves). The data along the constant angle paths from MM are superimposed (dotted lines).

MM's 5–10 degree representation in V1 is similar to the conventional measurements, but the peripheral representation is expanded. Consider the distance between the 10 and 12 deg representations. In the control population, this distance ranges between 3–5 mm. In MM's left hemisphere this distance

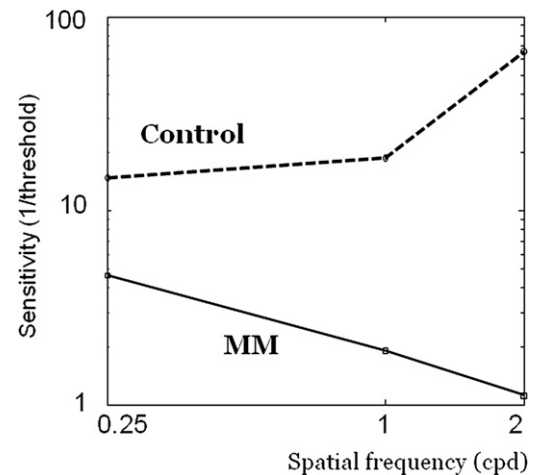


Figure 1. A Comparison of the Contrast Sensitivity Function (CSF) in MM and a Typical Sighted Control

Subjects discriminated between briefly (500 ms) flashed horizontal and vertical Gabor patches. The stimuli were presented at fixation, and the Gabor was windowed to a diameter of 4 deg of visual angle. Stimulus contrast threshold was measured using an interleaved staircase design: stimulus contrast was increased after an error or decreased after two correct. The staircase continued until each spatial frequency targets had at least 8 reversals; contrast sensitivity is the inverse of the mean contrast at the staircase reversals. MM has no sensitivity to contrast patterns beyond 2 cpd, as previously reported in Fine et al. (2003). For this Gabor stimulus the typical normal control is one to two orders of magnitude more sensitive.

is 5 mm and in his right hemisphere the distance is about 8.5 mm, nearly double the control value. Hence, compared to normal controls he has more cortical area devoted to the representation of the visual field beyond 10 deg eccentricity.

V1 Population Receptive Field Sizes in MM Differs from Controls

The population receptive field (pRF) estimates the region of the visual field that effectively stimulates a response in a small region of visual cortex. The pRF is a Gaussian model in which the center and size of the Gaussian are estimated by fitting the model to the responses from moving bar stimuli (Figure 3). The pRF fits in many parts of MM's visual cortex were very good, explaining 48% of the time series variance in V1 (Figure 3, upper panel) and 57% of the time series variance in LO (Figure 3, lower panel). Similar to controls, MM's pRF sizes increases from V1 to V3 (Figure 4). Also like controls, the pRF sizes in LO are much larger than those in early cortical areas (Figure 3, right side).

Measured quantitatively, we see that MM's pRF data in V1–V3 differ from controls in two ways (Figure 4). First, estimated pRF sizes are generally larger than controls at eccentricities from 8–12 deg. Second, in controls the pRF size increases with eccentricity. But, in MM the pRF size declines over the eccentricity range from 8–12 deg. As we discuss below, MM's unusual pRF sizes and V1 map may be explained by a lack of cortical neurons with small receptive fields.

Extrastriate Responses Represent Central Vision

Despite the very limited foveal representation in V1–V3, there are substantial central responses in dorsolateral extrastriate regions (Figure 5; see a ventral foveal response in Figure 2, as well).

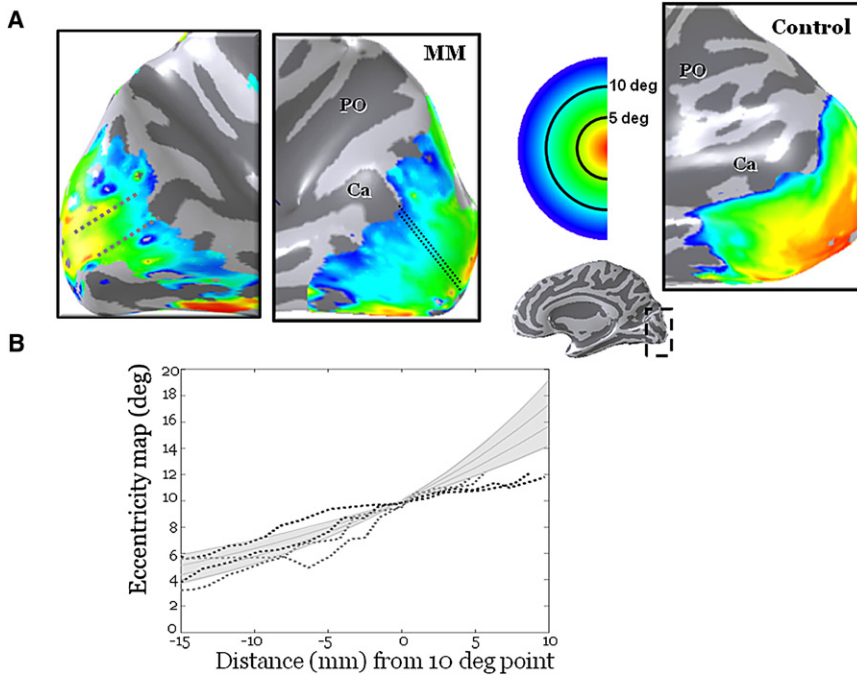


Figure 2. Visual Field Eccentricity Maps Near MM's Calcarine Sulcus

(A) Eccentricity maps on the medial aspect of the right and left hemisphere in MM (left) and a control (right). The region of interest near calcarine and a color map defining the visual field eccentricity are shown in the inset at the middle. The measurements mapped the central 14 degrees of MM's visual field. There is an organized eccentricity map (green to blue) in MM's anterior calcarine. The data are shown on smoothed images of occipital cortex; dark shading is within a sulcus and light shading a gyrus. Ca = calcarine sulcus, PO = parieto-occipital sulcus.

(B) Visual field eccentricity in V1 measured as a function of distance from the 10° representation. Individual curves are measured along four line ROIs selected to fall on iso-angle representations (black for the right, gray lines for the left; the line ROIs are shown in the upper left images). The solid lines represent a function that fits to the eccentricity versus distance in control population data, $\text{ecc} = \exp(d^* x + \ln(10))$. The parameter x is the distance along the calcarine (millimeters) and d is a scale factor that varies between individuals, ranging between 0.035 and 0.07, which covers the range of normal observers we have measured in our laboratory, represented by the gray shaded region (Dougherty et al., 2003).

The locations of MM's extrastriate foveal representations are comparable to those in control subjects (see also Wandell et al., 2005, Figures 5 and 7; Wandell et al., 2007, Figure 9). The most glaring differences between MM's visual field maps and those of controls are the very large cortical surface area spanned by the extrastriate foveal responses. In the Discussion, we consider how these representations might arise in the absence of near-foveal V1 responses.

Fixation Stability Does Not Explain Abnormal Cortical Responses

The possibility that fixation instability would be the source of the pRF and eccentricity map differences can be ruled out for several reasons. First, fixation instability introduces a common increase in pRF size across all eccentricities; it does not differentially affect receptive fields sizes across different eccentricities, or receptive field sizes in one part of cortex. The pRF sizes in the near periphery (10 deg) are normal, suggesting that fixation instability is not significant. Second, MM's fixation stability was evaluated previously and reported as nearly normal (Fine et al., 2003). Third, we analyzed the potential influence of MM's recorded eye movements' on pRF size through simulation (Figure 6). The calculations comprised three parts. First, we estimated the pRF model for a control observer with very stable fixation using the same stimuli as we used for MM. The map and pRF size estimates are shown in Figure 6A. Second, we created a set of simulated data for the control observer using this model and assuming a stimulus that incorporated MM's eye movements (Figure 6D). Third, we estimated the pRF sizes and eccentricity map from the simulated data (Figure 6B). The maps and pRF sizes estimated from the data with MM's simulated eye movements did not differ significantly from the original map (i.e., the

same foveal representation). When the simulated eye movements are exaggerated beyond those in MM (Figure 6E), the simulation shows a clear increase in the estimated pRF size (Figure 6C). This increase is present across V1. Even with large eye movements, the V1 map can still be estimated.

White Matter Mapping

During the critical period synaptic circuitry is formed along with the myelo-architecture that supports the axons and intracortical communication. We investigated the microstructure of MM's white matter pathways to search for further clues about MM's developmental failures.

We assess white matter integrity using directional diffusivity measures. By measuring diffusivity in multiple directions we obtain estimates of the principal diffusion direction (longitudinal) as well as the perpendicular direction (radial). The ratio of these two values is similar to the fractional anisotropy (FA).

Specific disruptions of the white matter produce specific disruptions in the diffusion signal. For example, Song et al. (2003), using animal models of acute CNS injury, have demonstrated that longitudinal and radial diffusivities within white matter tracts correlate with axon and myelin pathologies, respectively. Unfortunately, the reverse inference is not possible: distinct types of white matter disruptions can produce similar diffusivity change (Paus, 2010). Hence, at this time measurements of diffusivity differences cannot be interpreted unambiguously with respect to developmental failures.

Reduced Longitudinal Diffusivity in MM's Optic Tract

MM's optic tracts, running from the optic chiasm to the lateral geniculate nucleus (white sphere), are shown as the blue fascicles (Figure 7A). The scatter plot compares the radial and

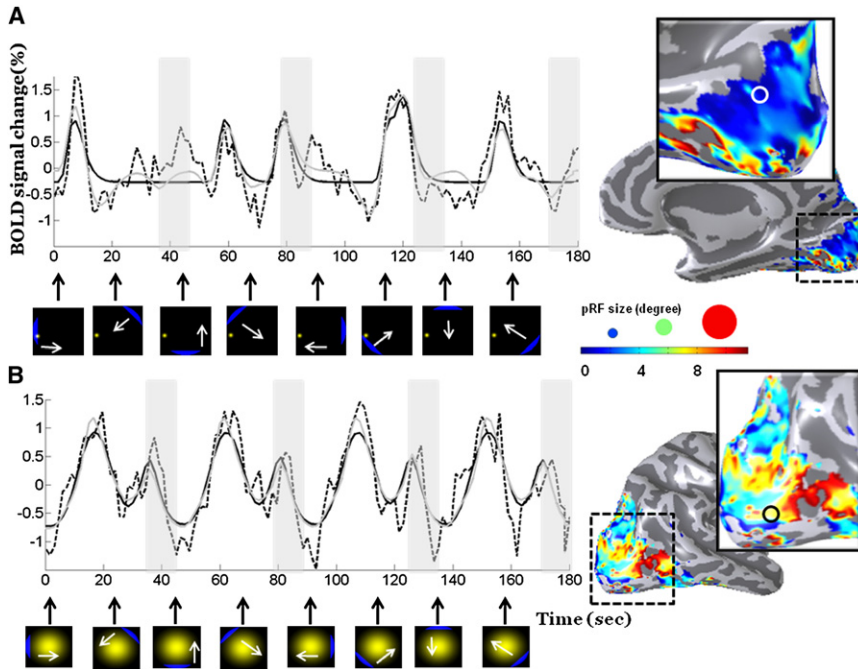


Figure 3. Population Receptive Field (pRF) Models of the Cortical Responses

The pseudo-color maps on the right show estimated pRF-size on the medial (upper) and lateral (lower) occipital cortex. The graphs show BOLD time-series (dashed) and model predictions (solid) from a voxel located in V1 (upper) and another in lateral occipital (lower) cortex. The white and black circles on the maps indicate the positions of the selected voxels; these voxels were typical of their respective regions. Predictions for an isotropic two-dimensional (2D) single Gaussian model (black) and a center-surround two-Gaussian model (gray) are shown. The white portions of the graph indicate time periods when the bar was moving in the visual field; the gray-shaded regions indicate times when only the mean luminance field was presented.

(A) In V1 the single-Gaussian population receptive field model explains 48% of the variance in the time course data. The two-Gaussian model explains 56% of the time course data and improves the fit in regions when the BOLD signal becomes negative. There is an interesting deviation between the predicted and observed V1 time course. In two of the mean luminance blocks, there is a significant V1 activation even though no stimulus is present (45 s and 90 s). We have also

noted such responses in normal controls. Both the one- and two-Gaussian models fail to predict these responses because the model responses are driven entirely by the stimulus. The explanation for these signals must arise from non-stimulus events, such as the subject's expectations.

(B) In LO a single-Gaussian model explains 57% of the time series variance; there is no improvement using the two-Gaussian model. This LO signals are driven by population of neurons whose receptive field sizes cover a much larger portion of the visual field than the V1 neurons, and the stimulus never completely leaves the pRF. Consequently, the model predicts and we measure eight peaks in the BOLD time series. The amplitude of the peak; however, is reduced whenever the stimulus is replaced by a mean luminance stimulus. The small images at the bottom of each graph show the estimated position and size of the pRF (yellow spot), the position of the stimulus bar (blue line), and the direction the bar was moving (white arrow). The black arrows indicate the times when the bar changed its motion direction. The pRF size scale bar is an inset at the right.

longitudinal diffusivity in MM with normally sighted controls, two monocular subjects, and a blind subject. Each point shows the average of the right and left optic tract, which did not differ signif-

icantly. The fractional anisotropy (FA) of the normally sighted controls falls within a small range (0.465 ± 0.05 ; see [Table S1](#) available online). MM's mean FA (0.414) does not differ

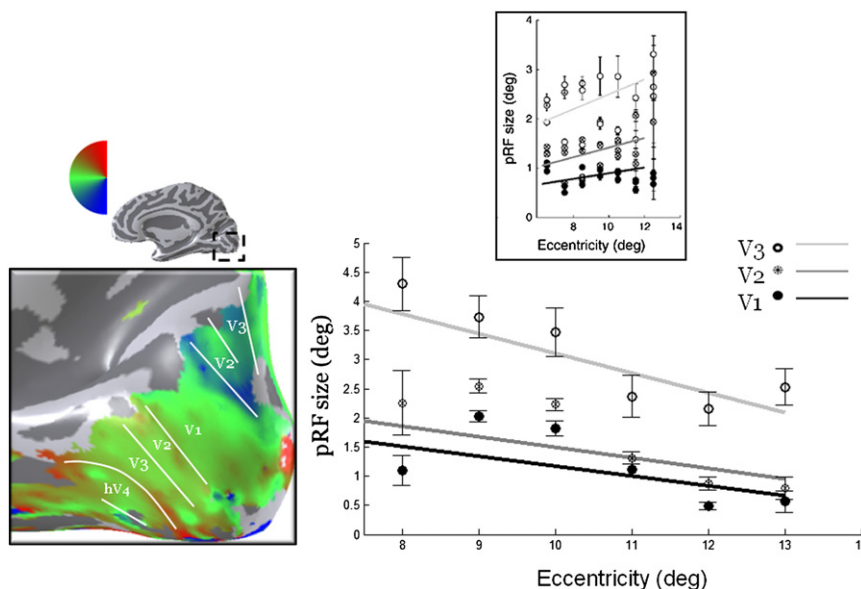


Figure 4. The Relationship between Eccentricity and pRF Size in V1-V3

The image at the left shows angle maps for MM on his smoothed right occipital lobe. Reversals in the angular representation define the boundaries between maps and are identified by the solid white lines. The main graph shows MM's estimated population receptive field sizes as a function of eccentricity. Different symbols indicate estimates from V1, V2, and V3. For comparison, average pRF-size estimates from three control subjects are shown in the inset. Solid lines are fit to the points from each map. In controls and MM, pRF-size increases systematically from V1 to V3. MM's estimated receptive field sizes at eccentricities from 8-10 deg are larger than those in controls. The pRF sizes beyond 10 deg are similar or smaller compared to controls. Color inset upper left: the angular representation.

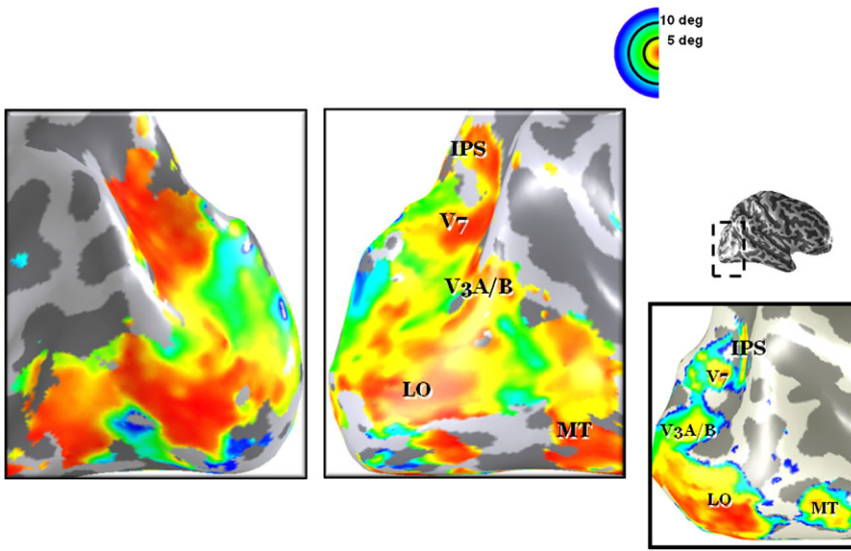


Figure 5. Visual Field Eccentricity Representations in Medial-Ventral and Dorsal-Lateral Cortex

Visual field eccentricity maps in lateral-occipital surface of MM's left (left panel) and right (right panel) hemispheres. Several extrastriate regions respond powerfully to foveal stimuli. The right hemisphere regions of interest, an example map of a control subject, and a color map defining the visual field eccentricity representations are shown at the right. IPS = intra-parietal sulcus; LO = lateral occipital. Other details as in Figure 2.

significantly from the controls. However, MM's left and right longitudinal diffusivities are lower than that of the normally sighted controls, and MM's average diffusivities are outside the 3 SD (figure shows 2 SD covariance) covariance ellipsoid of the normal population.

The optic tract measurements of the two monocular subjects are in the distribution of the normal population. Thus, the fact that MM is monocular would not ordinarily have placed him outside the normal distribution. The early blind subject, like MM, is outside the normal range.

We also performed a whole brain statistical analysis (Schwartzman et al., 2005) comparing the ellipsoidal orientations

and axis lengths in MM with a control group of 30 sighted adults (aged 19–53, 20 males). There were no differences in the orientations, consistent with the principal that MM has all of the major pathways present in controls. There were differences in the axis lengths, confirming the ROI based analysis. Specifically, the whole-brain comparison shows a significant diffusivity difference ($p < 0.005$) in and near the optic chiasm (Figure S1D).

Diffusivity in MM's Optic Radiation Differs Marginally from Controls

MM's optic radiation, including Meyer's loop, was identified using ConTrack (Sherbondy et al., 2008a). The scatter plots in Figure 7B compare MM's radial and longitudinal diffusivity with that of controls. In all subjects the radial diffusivity in the right optic radiation is larger than the left (Sherbondy et al., 2008b). In controls, the optic radiation longitudinal diffusivity is near the maximum value found in white matter ($2 \mu\text{m}^2/\text{ms}$); but MM's

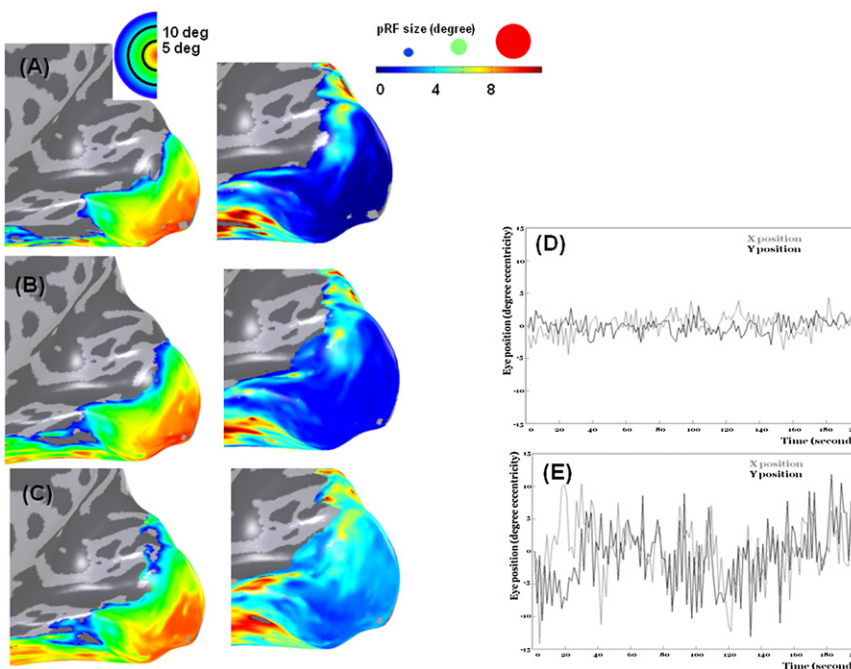


Figure 6. The Effect of Simulated Eye Movements on Visual Field Eccentricity Maps and Population Receptive Field (pRF) Sizes

Eccentricity maps (left column) and population receptive field sizes (middle column) are presented on the medial aspect of the right hemisphere. Data from a normal control (upper row) were used to estimate a complete pRF model. We added simulated eye movements from MM to this model (middle row) or an exaggerated form of these movements ($4\times$ larger than MM's observed eye movements; bottom row) and again estimated the maps and pRF size. The organized eccentricity map with its large confluent foveal representation (red-orange) is evident in both simulations; the population receptive field size increases at all eccentricities. The x and y eye-movements for MM, and the exaggerated version of these movements are shown on the right panels.

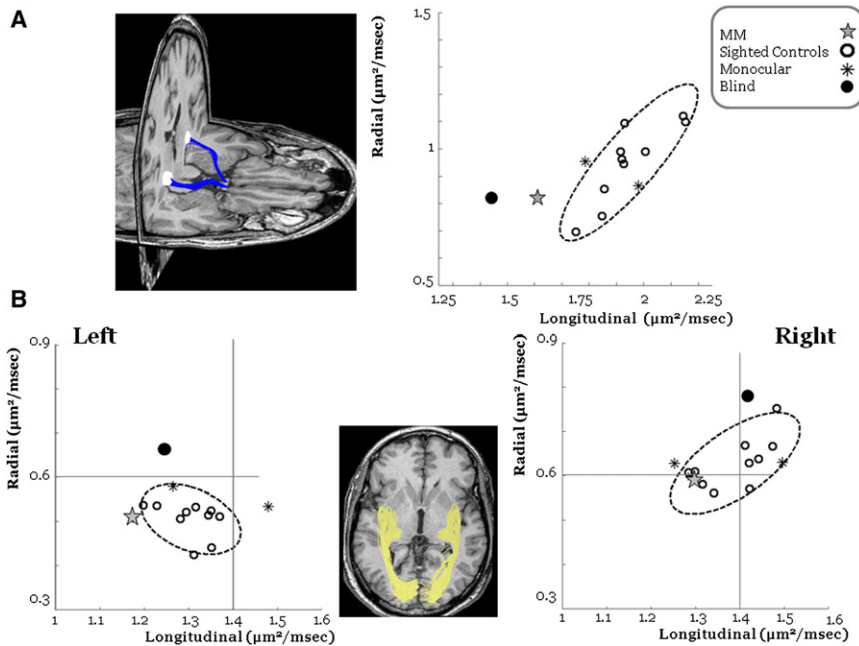


Figure 7. Comparison of Radial and Longitudinal Diffusivities in the Optic Tracts and Optic Radiations

(A) Three-dimensional rendering of the optic tract fibers (blue) shown superimposed on axial and coronal slices of MM's brain; note the missing left eye. The optic tracts connect the optic chiasm and the LGN (white sphere). Scatter plot of the radial and longitudinal diffusivities for the average of the right and left tracts optic tracts. Data are from MM (gray star), 10 normal controls (black open circles), 2 seeing monocular subjects (black asterisks) and one blind subject (black closed circle). The 2 standard deviation covariance ellipsoid (dashed) is shown.

(B) Rendering of the optic radiation (yellow) shown superimposed on an axial slice of MM's brain viewed from below. The two scatter plots compare radial and longitudinal diffusivities in the right and left optic radiations. The symbol types are the same as in (A). A 2 standard deviation covariance ellipsoid (dashed) is shown for each graph. See also Figure S1 and Table S1.

longitudinal diffusivity is low and his data are on the border of the 2 SD covariance ellipsoid. The right-left difference between the optic radiations may be caused by different patterns of the crossing fibers in the two hemispheres. MM's mean FA (0.48) does not differ significantly from the normally sighted control group (0.5 ± 0.05 SD).

The diffusivities of the blind subject are well outside the normal range due to a very large value in right and left radial diffusivity. Diffusivity in the monocular subjects is at the margin or outside the 2D ellipsoid defined by the normally sighted controls. Table S1 summarizes FA and mean diffusivity (MD) values for all subjects.

Unusually Small Cross-Sectional Area of Interhemispheric Occipital Connections

We used fiber tractography to estimate the cross-sectional area of the occipital fibers that connect right and left visual cortex (Figure 8). In normal controls there is a correlation between the cross-sectional area of this tract and the cross-sectional area of the entire callosum ($r = 0.53$). For the two monocular subjects, the cross-sectional area of the occipital callosal fibers is within the distribution of the normal population. Both the blind subject and MM have small occipital-callosal fiber cross-sections. For the blind subject, who has a small corpus callosum, the small occipital-callosal cross-section is about equal to the size

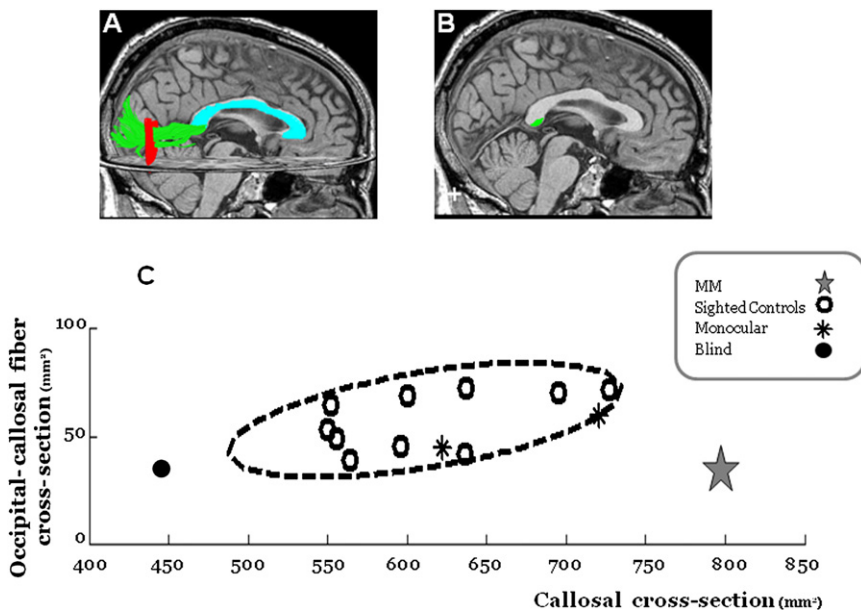


Figure 8. The Interhemispheric Occipital-Callosal Fibers Cross-Sectional Area Is Small

(A) Fibers are tracked from seed points in the entire hemisphere. Those that intersect with the corpus callosum are identified. A region of interest is selected in the occipital lobe (red region). The subset of occipital-lobe fibers that pass through the corpus callosum (cyan) are identified (green).

(B) The location of the occipital-callosal fibers in the plane of the corpus callosum.

(C) Scatter plot of the cross-sectional area of the occipital callosal fiber group in relation to the cross-sectional area of the corpus callosum. The 2 standard deviation covariance ellipsoid (dashed) is shown. The cross-sectional area of MM's occipital-callosal fiber group (gray star) is smaller than that of controls (open circles) and the monocular subjects (black asterisks) while the overall size of his corpus callosum is very large. The occipital cross-sectional area of the blind subject (black filled circle) is small too.

See also Figure S2.

predicted from extrapolating the control data. For MM, who has a large corpus callosum, the occipital-callosal fiber cross-section is quite small and inconsistent with the correlation observed in the normal population.

While the area of the occipital callosal group is small in MM, his radial and axial diffusivities along this fiber tract are within the distribution of the controls (Table S1).

Normal Callosal-MT⁺ Pathways

fMRI responses and surface area in MM's motion complex (MT⁺) are similar to those in controls (Fine et al., 2003). Here, we further measured the MT⁺ pathways to the callosum to determine whether the white matter circuitry also matched normal controls. We found the most likely pathway between MT⁺ and the callosum; MT⁺ was identified using a standard fMRI motion localizer. In MM these pathways follow precisely the same pattern we described in an earlier analysis (Sherbondy et al., 2008a): the callosal connections pass by the dorsal surface of the lateral ventricle and cross the callosum in the dorsal portion of the splenium (Figure S2). While there is no formal atlas of these fibers in controls, we have examined 30 examples of such pathways and the MT-callosal pathway in MM is quite typical, consistent with the BOLD responses and good motion perception.

DISCUSSION

Abnormal Cortical Maps

We observed three unusual features of MM's visual field map organization. First, there is an atypical eccentricity map in V1. Second, the estimated population receptive field sizes in MM's near-foveal representation of V1 are almost twice those in controls and decrease, rather than increase, with eccentricity. Third, we were unable to measure a V1 foveal response, but we could measure unusually large foveal representations in VO, LO, MT⁺ and the IPS clusters.

There is a hypothesis that might explain both the large V1 pRF sizes and the prominent extrastriate foveal signals. We speculate that MM is selectively missing V1 neurons with small receptive fields. These cells may have been lost because at the time of his accident, these cells were not fully mature (Mayer and Dobson, 1982; Kiorpes and Movshon, 1989; Skoczenski and Norcia, 2002). The development of the small retinogeniculate receptive fields that signal high spatial frequency information, which are typically found in foveal V1, may require retinal contrast in the spatial frequency range beyond that present in MM's retina. Consequently, it is possible that in MM only those neurons with relatively large receptive fields survived.

This speculation explains three aspects of MM's data. First, MM has very poor spatial frequency resolution compared to normal controls (Fine et al., 2003). We confirmed that MM continues to have poor spatial resolution even seven years following his operation (Figure 1).

Second, in normal development, there are many neurons with small receptive fields; these compete with the large receptive field population and extrastriate feedback for synaptic space in V1. If the small receptive field neurons are absent in MM's V1, and their synaptic space is given over to these large receptive field neurons, we expect to find large V1 pRF sizes.

Third, the loss of cells with small receptive fields may allow extrastriate feedback projections to obtain more synaptic space than normal. This increase would be particularly significant in the foveal representation where there is ordinarily the highest density of neurons with small receptive fields. This extra space may lead to an upregulation of the foveal extrastriate signals with a foveal projection. This upregulation could explain the large foveal extrastriate responses.

Diffusivity Changes in Visual Pathways

Major tracts of the visual system (superior colliculus, optic tract, and optic nerve) are present and begin to myelinate prior to birth; the myelination process is mature by 9 months of age (Webb et al., 2001). MM was normally sighted until 3 years of age, and we confirm that MM's optic tract and optic radiation are present and identifiable.

The loss of one eye combined with the loss of retinal image contrast in the intact eye affected MM's optic tract diffusivity. The effects of eye damage via retinal ischemia on diffusivity were studied in a mouse model. In mouse, most of the axons in each optic nerve cross (95%–97%) so that the optic tract is a continuation of the contralateral optic nerve. Retinal ischemia produced sustained reduction of longitudinal diffusivity in the ipsilateral optic nerve (Song et al., 2003) and the contralateral optic tract (Sun et al., 2008). Immunohistochemistry suggests that the longitudinal diffusivity decrease is caused by axonal damage (Sun et al., 2008). The diffusivity difference may not be present in human optic tract because, unlike mouse, each human optic tract is composed of nerves from both eyes.

A human postmortem case report illustrates anterograde axonal degeneration in one optic nerve, both optic tracts, and the eye-specific neuronal lamina in both LGNs following enucleation of one eye (Beatty et al., 1982). We conclude that diffusion weighted measurements are not sensitive enough to detect such changes in monocular subjects, whereas MM's monocularly combined with reduced retinal image contrast creates changes that are sufficient to be detected by diffusion imaging.

Shimony et al. (2006) report that there is an approximately 40% decrease in the white matter volume adjacent to V1 and V2 in early blind (see also Pan et al., 2007). This white matter would normally include the optic radiation. Two groups found severely atrophied or simply missing optic nerves/chiasm/tracts/radiation in congenitally blind human subjects (Shimony et al., 2006; Ptito et al., 2008). We also found significant white matter differences between the controls and the blind subject, who lost his vision at 10 months. Using ConTrack, we could find the blind subject's optic radiations. The radial diffusivity in the optic radiation of the early blind is higher than in controls, and this may reduce the effectiveness of the streamline tracking method used by other groups.

We can identify MM's visual pathways, but even 7 years after surgery that restored MM's retinal image contrast, the longitudinal diffusivity in MM's optic tract differs from controls. This difference is not present in monocular controls, supporting the hypothesis that the reduced longitudinal diffusivity is caused by the early loss of functional signals (Fields, 2005).

Occipital-Callosal Fiber Group Size Is Reduced

The size of the posterior regions of the corpus callosum increases throughout adolescence (Giedd et al., 1999). MM's occipital-callosal fiber group has a small area, which may be due to arrested development of the posterior callosum. During development, there may be competition for synaptic space between different types of systems, such as visual and auditory modalities. In the absence of a powerful visual input, visual fibers may acquire less synaptic space. In kittens, binocular visual deprivation by eye enucleation or eyelid suture reduces the number of visual callosal axons; the remaining axons are thinner than normal controls and have decreased number of branches and synaptic boutons (Innocenti, 2007). If the occipital-callosal fibers are purely visual, and MM's visual pathways lost synaptic space to non-visual systems, this would explain why MM's occipital-callosal fiber cross-section is small compared to the overall size of his callosum. The hypothesis that non-visual modalities have expanded signals is supported by a report that in MM, but not in controls, MT⁺ responds to non-visual-motion input (Fine et al., 2003; Saenz et al., 2008).

Conclusion

The literature on adult cortical plasticity following damage or deprivation is substantial and includes a wide array of reports in both human and animal models (Wandell and Smirnakis, 2009). Following peripheral damage some measures show adult cortical stability (Smirnakis et al., 2005; Adams et al., 2007) and others plasticity (Gilbert and Wiesel, 1992; Baker et al., 2005). There are also reports showing that behavioral training can improve performance following cortical damage (Huxlin et al., 2009). Behaviorally, MM's inability to recover high quality visual perception matches the difficulties described in other subjects (Valvo, 1971; Gregory, 1963). In MM's case, we have been able to apply modern neuroimaging methods to explore the significant anatomical and functional differences in the brain.

The neuroimaging data suggest a specific cause of the limited recovery. MM's vision was interrupted at a time when visual neurons with small receptive fields were developing (Mayer and Dobson, 1982; Skoczenski and Norcia, 2002). We suggest that the injury prevented this important class of neurons from stabilizing during development because the retinal image contrast needed to stimulate these neurons was eliminated by his optics. Because these neurons are important inputs to the ventral pathways of the brain, used for object recognition, MM has both poor resolution and limited ability to interpret objects.

We rely on the premise that normal development involves neural competition for synaptic space to understand the loss of these cells on MM's brain. We propose that unbalanced competition between different parts of the visual systems (small versus large receptive fields) and competition between different sensory systems (visual and nonvisual), produce an unusual functional and structural brain architecture that is inadequate to perform key perceptual functions, such as object recognition.

While we detect the absence of small receptive fields using cortical measurements, the neural basis may be retinal. Support for the retinal hypothesis comes from the diffusivity measurements in the optic tracts which show that MM's retinal axons differ from controls and sighted monocular subjects. These

differences might be due to a reduced number of small retinal ganglion cells that normally carry fine detail information. During development small perturbations in the retina can lead to large-scale cortical reorganization (Baseler et al., 2002). There are several reports that blind visual cortex is colonized by other modalities (Sadato et al., 1996; Amedi et al., 2003) and in MM's case there is a specific report that unlike controls MT⁺ responds to nonvisual-motion input (Fine et al., 2003; Saenz et al., 2008).

MM's case illustrates that restoration of functional vision requires more than improving retinal image contrast. It is necessary to account for the subject's developmental trajectory and the consequences of early deprivation on cortical circuitry. The new methods described here, including pathway tracking with DTI, visual field maps and receptive field estimation should be helpful tools in the clinical assessment of the possibilities for successful intervention.

EXPERIMENTAL PROCEDURES

Subject

Subject MM, a 53-year-old male, lost his left eye and became blind in the right eye after chemical and thermal damage to the cornea and surrounding limbal stem cells at the age of 3 years. He had some light perception, but no experience of contrast or form. One unsuccessful corneal replacement was attempted in childhood, but he reported no visual memories or imagery. At age 46, MM received a corneal and limbal stem-cell transplant in his right eye.

The study was approved by the Stanford Institutional Review Board and informed written consent was obtained from all subjects.

fMRI

Stimulus Presentation

Visual stimuli were generated in Matlab using the Psychophysics Toolbox (Brainard, 1997; Pelli, 1997) on a Macintosh G4 Powerbook. The display configuration consisted of an LCD projector (NEC LT158) with optics that imaged the stimuli onto a back-projection screen in the bore of the magnet. The screen was viewed via a front-surface mirror mounted to the head coil.

Stimuli

We used retinotopic mapping stimuli that consisted of high-contrast, flickering, checkerboards in a rotating wedge and expanding ring (Engel et al., 1997). The stimuli moved in a periodic pattern and completed a full cycle in 24 s with a total of six cycles per scanning run. The wedge subtended 45° and the rings were 3.5° thick (1/4th of the maximum stimulus radius). Mean-luminance periods were inserted at a different rate (4 cycles/scan) than the rotating wedge or expanding ring cycles (6 cycles/scan). The stimulus eccentricity ranged up to 14° of visual angle. Using this method, each mean-luminance presentation replaces a different position of the wedge or ring stimulus.

Additionally, we measured responses to drifting checkerboard patterns seen through a moving bar aperture. The bar width subtended 3.5° and subtended one period (black and white square) of the checkerboard. During a scan the bar traverses the visual field in eight directions; there was no repetition of any bar stimulus within a single scan. Four interleaved periods of mean luminance (zero contrast) were included in these scans. If the bar is never replaced with a mean luminance stimulus we expect eight peaks in the BOLD response, corresponding to each time the bar passes through the pRF. If the pRF is small, replacing the stimulus with a mean luminance should eliminate three peaks in the BOLD response.

Fixation was controlled by having the subject monitor a large fixation point and reporting an occasional and unpredictable change in color. The full field of view of this stimulus set was 14° of visual angle.

Data Acquisition

Magnetic resonance images were acquired with a 3T General Electric Signa scanner with a custom-designed surface coil (Nova Medical, Wilmington, MA) centered over the subject's occipital pole. Foam padding and tape minimized head motion. Functional MR images (TR/TE 1500/30 ms, flip angle

55°) were acquired using a self-navigated spiral-trajectory pulse sequence (Glover and Lai, 1998) with 20 slices oriented orthogonal to the calcarine sulcus. The effective voxel size was $2.5 \times 2.5 \times 3 \text{ mm}^3$ (FOV = $24 \times 24 \text{ cm}^2$) with no slice gap. Functional scans using wedge or ring stimuli were acquired using 104 time frames (scan duration of 2.6 min). Functional scans using bar stimuli were acquired using 128 time frames (3.2 min). T1-weighted anatomical MR images were acquired using a fast spoiled gradient echo (SPGR) sequence prior to the functional scans and the same slice prescription as the functional scans.

In a separate session, high-resolution T1-weighted images were acquired on a 1.5 T Signa LX scanner with a vendor-supplied head-coil using a 3D-SPGR pulse sequence (1 echo, minimum TE, flip angle 15°, effective voxel size of $0.94 \times 0.94 \times 1.2 \text{ mm}^3$).

Data Analysis

Anatomical Images. T1-weighted anatomical MRI data sets were averaged and resampled to a 1 mm^3 isotropic resolution. The surface-coil anatomical MRI, taken at the same time as the functional images and thus co-registered with them, was aligned with the previously acquired head-coil anatomical MRI. Gray and white matter was segmented from the anatomical MRI using custom software and hand-edited to minimize segmentation errors (Teo et al., 1997). The cortical surface was reconstructed at the white/gray matter border and rendered as a smoothed 3D surface. Functional images (Wandell et al., 2000).

The first eight time-frames of each functional scan were discarded due to start-up magnetization transients. The remaining time-frames were motion corrected (Nestares and Heeger, 2000); no spatial or temporal smoothing was performed.

Population Receptive Field Analysis. This method computes a model of the population receptive field (pRF) at each location in cortex from responses to a wide range of stimuli. Each pRF is modeled as a circularly symmetric Gaussian receptive field in visual space. This receptive field is defined by three parameters: spatial position of the center (x, y) and receptive field size (σ). Once the parameters are set, we can make a specific prediction of the BOLD time series; the parameters are estimated by finding the values that minimize the difference between the predicted and observed time series. Detailed description of the pRF method are described in Dumoulin and Wandell (2008). All the custom image processing software used for this analysis is available as part of our open-source mVista package available for download (<http://vistalab.stanford.edu/software/>).

DTI

Subjects

Diffusion tensor imaging (DTI) data was collected on MM and 10 controls with normal vision aged 32–53 (four females). We also obtained data from two monocular subjects and a blind subject. The monocular subjects were a 31-year-old male who lost his right eye (due to trauma) when he was 6 years old, and a 50-year old male who lost his left eye when he was 2 years old. Visual function in the remaining was intact. The blind subject was a 56-year-old male who lost both eyes (retinoblastoma) when he was 10 months old.

Data Acquisition

DTI data were acquired on a 1.5T Signa LX (Signa CVi; GE Medical Systems, Milwaukee, WI) with a self-shielded, high-performance gradient system capable of providing a maximum gradient strength of 50 mT/m at a gradient rise time of 268 μs for each of the gradient axes. A standard quadrature head coil was used for excitation and signal reception. The DTI protocol used eight 90 s whole-brain scans. The pulse sequence was a diffusion-weighted, single-shot, spin-echo, echo-planar imaging sequence (echo time, 63 ms; repetition time, 6 s; field of view, 260 mm; matrix size, 128×128 ; bandwidth, $\pm 110 \text{ kHz}$; partial k-space acquisition). We acquired 48–54 axial, 2 mm thick slices (no skip) for two b values, $b = 0$ and $b = 800 \text{ s/mm}^2$. The high b value was obtained by applying gradients along 12 different diffusion directions (six noncollinear directions). Two gradient axes were energized simultaneously to minimize echo time. The polarity of the effective diffusion-weighting gradients was reversed for odd repetitions to reduce cross-terms between diffusion gradients and imaging and background gradients.

Data Analysis

Preprocessing. Eddy current distortions and subject motion in the diffusion-weighted images were removed by a 14-parameter constrained nonlinear

coregistration based on the expected pattern of eddy current distortions given the phase-encode direction of the acquired data (Rohde et al., 2004). Each diffusion-weighted image was then registered to the mean of the (motion-corrected) non-diffusion-weighted images using a two-stage coarse-to-fine approach that maximized the normalized mutual information. The mean of the nondiffusion weighted images was also automatically aligned to the T1 image using a rigid body mutual information algorithm. All raw images from the diffusion sequence were then re-sampled to 2 mm isotropic voxels by combining the motion correction, eddy current correction, and anatomical alignment transforms into one omnibus transform and resampling the data using a 7th-order b-spline algorithm based on code from SPM5 (Friston and Ashburner, 2004). An eddy current intensity correction (Rohde et al., 2005) was also applied to the diffusion weighted images at this resampling stage. We note that the 7th-order b-spline interpolation does not require image variance correction (Rohde et al., 2004, 2005) due to the large support kernel. The rotation component of the omnibus coordinate transform was applied to the diffusion-weighting gradient directions to preserve their orientation with respect to the resampled diffusion images.

The tensors were fit using a least-squares algorithm. The eigenvalue decomposition of the diffusion tensor was computed, and the fractional anisotropy (FA) was calculated by using the resulting eigenvalues (Basser, 1995; Basser and Pierpaoli, 1996). The FA is the normalized standard deviation of the three eigenvalues and indicates the degree to which the isodiffusion ellipsoid is anisotropic. The mean diffusivity (MD) is the mean of the three eigenvalues, which is equivalent to one-third of the trace of the diffusion tensor.

Callosal Segmentation. To analyze diffusion properties in the corpus callosum, we used the segmentation procedure described elsewhere (Dougherty et al., 2007; Huang et al., 2005). Briefly, we segmented the corpus callosum based on the estimated cortical projection zone of the callosal fibers. The procedure was initiated by whole-brain fiber tracking, using a deterministic streamlines tracing technique (STT) algorithm (Basser et al., 2000; Conturo et al., 1999; Mori et al., 1999). Path tracing proceeded until the FA fell below 0.15 or until the minimum angle between the current and previous path segments was greater than 30°. This method produces many fiber paths for each hemisphere. We identified and retained the fibers that crossed the corpus callosum. The callosal segmentation procedure relies on a manually defined ROIs within the white matter. A region of interest is selected in the occipital lobe and the subset of fibers that pass through both the corpus callosum and this occipital lobe ROI are identified (Dougherty et al., 2007). We then measured the cross-sectional area of these callosal-occipital fibers in the plane of the corpus callosum. The process is repeated for both hemispheres. We also estimated the cross-sectional area of the whole corpus callosum.

Tract Identification. Deterministic tractography methods such as STT often miss smaller tracts such as the optic tract and optic radiation (Sherbondy et al., 2008a, 2008b). Therefore, we identified fibers in the optic tract and optic radiation using the ConTrack algorithm (Sherbondy et al., 2008a). This method is designed to find the most likely pathway between two regions of interest and has been validated against gold-standard postmortem tract-tracing methods (Sherbondy et al., 2008b).

Optic Tract. Optic chiasm ROIs were positioned on T1 maps of each subject. Both LGNs were also defined anatomically on the T1 maps, and their volume was standardized to 485 mm^3 . ConTrack calculated the most likely pathway between the ROIs of the optic chiasm and the LGN. A set of 5000 potential pathways were generated and the top 10% (500) highest scores fibers were chosen as the most likely pathways connecting these two regions.

Optic Radiation. We estimated the optic radiation as the most likely pathway between the LGN ROI and a functional estimate of V1. Because the distance between the LGN and V1 is greater than the distance from the chiasm to the LGN, and because the path is more complex, we sampled a larger collection of possible pathways (100,000). We estimated the optic radiation as the top 5% (5000) of these pathways. A few clearly misidentified fibers were eliminated (Sherbondy et al., 2008b).

MT⁺-Callosal Fibers. We estimated the most likely fibers between the functionally-defined MT⁺ and the corpus callosum. A set of 10,000 potential pathways were generated and the top 10% (1000) highest scores fibers were chosen as the most likely pathways connecting these two regions.

SUPPLEMENTAL INFORMATION

Supplemental Information includes two figures and one table and can be found with this article online at doi:10.1016/j.neuron.2009.12.006.

ACKNOWLEDGMENTS

This work was supported by NEI EY 03164 to B.A.W., Caesarea Edmond de Rothschild foundation to N.L., LLHF 2005/2BB to S.O.D., Michael Perry, Ione Fine.

Accepted: November 21, 2009

Published: January 13, 2010

REFERENCES

- Ackroyd, C., Humphrey, N.K., and Warrington, E.K. (1974). Lasting effects of early blindness. A case study. *Q. J. Exp. Psychol.* 26, 114–124.
- Adams, D.L., Sincich, L.C., and Horton, J.C. (2007). Complete pattern of ocular dominance columns in human primary visual cortex. *J. Neurosci.* 27, 10391–10403.
- Aguirre, G.K., Komáromy, A.M., Cideciyan, A.V., Brainard, D.H., Aleman, T.S., Roman, A.J., Avants, B.B., Gee, J.C., Korczykowski, M., Hauswirth, W.W., et al. (2007). Canine and human visual cortex intact and responsive despite early retinal blindness from RPE65 mutation. *PLoS Med.* 4, e230. 10.1371/journal.pmed.0040230.
- Amedi, A., Raz, N., Pianka, P., Malach, R., and Zohary, E. (2003). Early 'visual' cortex activation correlates with superior verbal memory performance in the blind. *Nat. Neurosci.* 6, 758–766.
- Baker, C.I., Peli, E., Knouf, N., and Kanwisher, N.G. (2005). Reorganization of visual processing in macular degeneration. *J. Neurosci.* 25, 614–618.
- Baseler, H.A., Brewer, A.A., Sharpe, L.T., Morland, A.B., Jägle, H., and Wandell, B.A. (2002). Reorganization of human cortical maps caused by inherited photoreceptor abnormalities. *Nat. Neurosci.* 5, 364–370.
- Basser, P.J. (1995). Inferring microstructural features and the physiological state of tissues from diffusion-weighted images. *NMR Biomed.* 8, 333–344.
- Basser, P.J., and Pierpaoli, C. (1996). Microstructural and physiological features of tissues elucidated by quantitative-diffusion-tensor MRI. *J. Magn. Reson. B* 111, 209–219.
- Basser, P.J., Pajevic, S., Pierpaoli, C., Duda, J., and Aldroubi, A. (2000). In vivo fiber tractography using DT-MRI data. *Magn. Reson. Med.* 44, 625–632.
- Beatty, R.M., Sadun, A.A., Smith, L., Vonsattel, J.P., and Richardson, E.P., Jr. (1982). Direct demonstration of transsynaptic degeneration in the human visual system: a comparison of retrograde and anterograde changes. *J. Neurol. Neurosurg. Psychiatry* 45, 143–146.
- Bi, A., Cui, J., Ma, Y.P., Olshevskaya, E., Pu, M., Dizhoor, A.M., and Pan, Z.H. (2006). Ectopic expression of a microbial-type rhodopsin restores visual responses in mice with photoreceptor degeneration. *Neuron* 50, 23–33.
- Brainard, D.H. (1997). The psychophysics toolbox. *Spat. Vis.* 10, 433–436.
- Carlson, S., Hyvärinen, L., and Raninen, A. (1986). Persistent behavioural blindness after early visual deprivation and active visual rehabilitation: a case report. *Br. J. Ophthalmol.* 70, 607–611.
- Conturo, T.E., Lori, N.F., Cull, T.S., Akbudak, E., Snyder, A.Z., Shimony, J.S., McKinstry, R.C., Burton, H., and Raichle, M.E. (1999). Tracking neuronal fiber pathways in the living human brain. *Proc. Natl. Acad. Sci. USA* 96, 10422–10427.
- Dougherty, R.F., Koch, V.M., Brewer, A.A., Fischer, B., Modersitzki, J., and Wandell, B.A. (2003). Visual field representations and locations of visual areas V1/2/3 in human visual cortex. *J. Vis.* 3, 586–598.
- Dougherty, R.F., Ben-Shachar, M., Deutsch, G.K., Hernandez, A., Fox, G.R., and Wandell, B.A. (2007). Temporal-callosal pathway diffusivity predicts phonological skills in children. *Proc. Natl. Acad. Sci. USA* 104, 8556–8561.
- Dumoulin, S.O., and Wandell, B.A. (2008). Population receptive field estimates in human visual cortex. *Neuroimage* 39, 647–660.
- Engel, S.A., Glover, G.H., and Wandell, B.A. (1997). Retinotopic organization in human visual cortex and the spatial precision of functional MRI. *Cereb. Cortex* 7, 181–192.
- Fields, R.D. (2005). Myelination: an overlooked mechanism of synaptic plasticity? *Neuroscientist* 11, 528–531.
- Fine, I., Wade, A.R., Brewer, A.A., May, M.G., Goodman, D.F., Boynton, G.M., Wandell, B.A., and MacLeod, D.I. (2003). Long-term deprivation affects visual perception and cortex. *Nat. Neurosci.* 6, 915–916.
- Friston, K.J., and Ashburner, J. (2004). Generative and recognition models for neuroanatomy. *Neuroimage* 23, 21–24.
- Giedd, J.N., Blumenthal, J., Jeffries, N.O., Rajapakse, J.C., Vaituzis, A.C., Liu, H., Berry, Y.C., Tobin, M., Nelson, J., and Castellanos, F.X. (1999). Development of the human corpus callosum during childhood and adolescence: a longitudinal MRI study. *Prog. Neuropsychopharmacol. Biol. Psych.* 23, 571–588.
- Gilbert, C.D., and Wiesel, T.N. (1992). Receptive field dynamics in adult primary visual cortex. *Nature* 356, 150–152.
- Glover, G.H., and Lai, S. (1998). Self-navigated spiral fMRI: interleaved versus single-shot. *Magn. Reson. Med.* 39, 361–368.
- Gregory, R. (1963). *Recovery from Early Blindness: A Case Study* (London: Heffer).
- Huang, H., Zhang, J., Jiang, H., Wakana, S., Poetscher, L., Miller, M.I., van Zijl, P.C., Hillis, A.E., Wytik, R., and Mori, S. (2005). DTI tractography based parcellation of white matter: application to the mid-sagittal morphology of corpus callosum. *Neuroimage* 26, 195–205.
- Huxlin, K.R., Martin, T., Kelly, K., Riley, M., Friedman, D.I., Burgin, W.S., and Hayhoe, M. (2009). Perceptual relearning of complex visual motion after V1 damage in humans. *J. Neurosci.* 29, 3981–3991.
- Innocenti, G.M. (2007). Subcortical regulation of cortical development: some effects of early, selective deprivations. *Prog. Brain Res.* 164, 23–37.
- Jacobson, S.G., Aleman, T.S., Cideciyan, A.V., Sumaroka, A., Schwartz, S.B., Windsor, E.A., Traboulsi, E.I., Heon, E., Pittler, S.J., Milam, A.H., et al. (2005). Identifying photoreceptors in blind eyes caused by RPE65 mutations: Prerequisite for human gene therapy success. *Proc. Natl. Acad. Sci. USA* 102, 6177–6182.
- Jiang, J., Zhu, W., Shi, F., Liu, Y., Li, J., Qin, W., Li, K., Yu, C., and Jiang, T. (2009). Thick visual cortex in the early blind. *J. Neurosci.* 29, 2205–2211.
- Kiorpes, L., and Movshon, J.A. (1989). Differential development of two visual functions in primates. *Proc. Natl. Acad. Sci. USA* 86, 8998–9001.
- Lagali, P.S., Balya, D., Awatramani, G.B., Münch, T.A., Kim, D.S., Busskamp, V., Cepko, C.L., and Roska, B. (2008). Light-activated channels targeted to ON bipolar cells restore visual function in retinal degeneration. *Nat. Neurosci.* 11, 667–675.
- Liu, Y., Yu, C., Liang, M., Li, J., Tian, L., Zhou, Y., Qin, W., Li, K., and Jiang, T. (2007). Whole brain functional connectivity in the early blind. *Brain* 130, 2085–2096.
- Mayer, D.L., and Dobson, V. (1982). Visual acuity development in infants and young children, as assessed by operant preferential looking. *Vision Res.* 22, 1141–1151.
- Merabet, L.B., Rizzo, J.F., Amedi, A., Somers, D.C., and Pascual-Leone, A. (2005). What blindness can tell us about seeing again: merging neuroplasticity and neuroprostheses. *Nat. Rev. Neurosci.* 6, 71–77.
- Mori, S., Crain, B.J., Chacko, V.P., and van Zijl, P.C. (1999). Three-dimensional tracking of axonal projections in the brain by magnetic resonance imaging. *Ann. Neurol.* 45, 265–269.
- Nestares, O., and Heeger, D.J. (2000). Robust multiresolution alignment of MRI brain volumes. *Magn. Reson. Med.* 43, 705–715.
- Ostrovsky, Y., Andalman, A., and Sinha, P. (2006). Vision following extended congenital blindness. *Psychol. Sci.* 17, 1009–1014.

- Pan, W.J., Wu, G., Li, C.X., Lin, F., Sun, J., and Lei, H. (2007). Progressive atrophy in the optic pathway and visual cortex of early blind Chinese adults: A voxel-based morphometry magnetic resonance imaging study. *Neuroimage* 37, 212–220.
- Park, H.J., Lee, J.D., Kim, E.Y., Park, B., Oh, M.K., Lee, S., and Kim, J.J. (2009). Morphological alterations in the congenital blind based on the analysis of cortical thickness and surface area. *Neuroimage* 47, 98–106.
- Pascual-Leone, A., Amedi, A., Fregni, F., and Merabet, L.B. (2005). The plastic human brain cortex. *Annu. Rev. Neurosci.* 28, 377–401.
- Paus, T. (2010). Growth of white matter in the adolescent brain: Myelin or axon? *Brain Cogn.*, in press. Published online October 22, 2009. 10.1016/j.bandc.2009.06.002.
- Pelli, D.G. (1997). The VideoToolbox software for visual psychophysics: transforming numbers into movies. *Spat. Vis.* 10, 437–442.
- Ptito, M., Schneider, F.C., Paulson, O.B., and Kupers, R. (2008). Alterations of the visual pathways in congenital blindness. *Exp. Brain Res.* 187, 41–49.
- Rohde, G.K., Barnett, A.S., Basser, P.J., Marengo, S., and Pierpaoli, C. (2004). Comprehensive approach for correction of motion and distortion in diffusion-weighted MRI. *Magn. Reson. Med.* 51, 103–114.
- Rohde, G.K., Barnett, A.S., Basser, P.J., and Pierpaoli, C. (2005). Estimating intensity variance due to noise in registered images: applications to diffusion tensor MRI. *Neuroimage* 26, 673–684.
- Sadato, N., Pascual-Leone, A., Grafman, J., Ibañez, V., Deiber, M.P., Dold, G., and Hallett, M. (1996). Activation of the primary visual cortex by Braille reading in blind subjects. *Nature* 380, 526–528.
- Saenz, M., Lewis, L.B., Huth, A.G., Fine, I., and Koch, C. (2008). Visual motion area MT+/V5 responds to auditory motion in human sight-recovery subjects. *J. Neurosci.* 28, 5141–5148.
- Schwartzman, A., Dougherty, R.F., and Taylor, J.E. (2005). Cross-subject comparison of principal diffusion direction maps. *Magn. Reson. Med.* 53, 1423–1431.
- Sherbondy, A.J., Dougherty, R.F., Ben-Shachar, M., Napel, S., and Wandell, B.A. (2008a). ConTrack: finding the most likely pathways between brain regions using diffusion tractography. *J. Vis.* 8, 15.1–15.16.
- Sherbondy, A.J., Dougherty, R.F., Napel, S., and Wandell, B.A. (2008b). Identifying the human optic radiation using diffusion imaging and fiber tractography. *J. Vis.* 8, 12.1–12.13.
- Shimony, J.S., Burton, H., Epstein, A.A., McLaren, D.G., Sun, S.W., and Snyder, A.Z. (2006). Diffusion tensor imaging reveals white matter reorganization in early blind humans. *Cereb. Cortex* 16, 1653–1661.
- Shu, N., Li, J., Li, K., Yu, C., and Jiang, T. (2009). Abnormal diffusion of cerebral white matter in early blindness. *Hum. Brain Mapp.* 30, 220–227.
- Skoczenski, A.M., and Norcia, A.M. (2002). Late maturation of visual hyperacuity. *Psychol. Sci.* 13, 537–541.
- Smirnakis, S.M., Brewer, A.A., Schmid, M.C., Tolia, A.S., Schüz, A., Augath, M., Inhoffen, W., Wandell, B.A., and Logothetis, N.K. (2005). Lack of long-term cortical reorganization after macaque retinal lesions. *Nature* 435, 300–307.
- Song, S.K., Sun, S.W., Ju, W.K., Lin, S.J., Cross, A.H., and Neufeld, A.H. (2003). Diffusion tensor imaging detects and differentiates axon and myelin degeneration in mouse optic nerve after retinal ischemia. *Neuroimage* 20, 1714–1722.
- Sun, S.W., Liang, H.F., Cross, A.H., and Song, S.K. (2008). Evolving Wallerian degeneration after transient retinal ischemia in mice characterized by diffusion tensor imaging. *Neuroimage* 40, 1–10.
- Teo, P.C., Sapiro, G., and Wandell, B.A. (1997). Creating connected representations of cortical gray matter for functional MRI visualization. *IEEE Trans. Med. Imaging* 16, 852–863.
- Valvo, A. (1971). *Sight Restoration after Long-term Blindness: The Problems and Behavior Patterns of Visual Rehabilitation* (New York: American Foundation for the Blind).
- Wandell, B.A., and Smirnakis, S.M. (2009). Plasticity and stability of visual field maps in adult primary visual cortex. *Nat. Rev. Neurosci.* 10, 873–884.
- Wandell, B.A., Chial, S., and Backus, B.T. (2000). Visualization and measurement of the cortical surface. *J. Cogn. Neurosci.* 12, 739–752.
- Wandell, B.A., Brewer, A.A., and Dougherty, R.F. (2005). Visual field map clusters in human cortex. *Philos. Trans. R. Soc. Lond. B Biol. Sci.* 360, 693–707.
- Wandell, B.A., Dumoulin, S.O., and Brewer, A.A. (2007). Visual field maps in human cortex. *Neuron* 56, 366–383.
- Webb, S.J., Monk, C.S., and Nelson, C.A. (2001). Mechanisms of postnatal neurobiological development: implications for human development. *Dev. Neuropsychol.* 19, 147–171.
- Weeks, R., Horwitz, B., Aziz-Sultan, A., Tian, B., Wessinger, C.M., Cohen, L.G., Hallett, M., and Rauschecker, J.P. (2000). A positron emission tomographic study of auditory localization in the congenitally blind. *J. Neurosci.* 20, 2664–2672.
- Yu, C., Shu, N., Li, J., Qin, W., Jiang, T., and Li, K. (2007). Plasticity of the corticospinal tract in early blindness revealed by quantitative analysis of fractional anisotropy based on diffusion tensor tractography. *Neuroimage* 36, 411–417.